Advanced Steel Construction – Vol. 17 No. 1 (2021) 39–49
DOI:10.18057/IJASC.2021.17.1.5

EXPERIMENTAL STUDY ON SEISMIC BEHAVIOR OF INNOVATIVE MULTI-CELLULAR CFT-WALLS WITH TIE-BOLTS

Gen-Shu Tong *, Chen-Hao Lin, Zhong-Zheng Hu and Shuang-Long Yang

Department of Civil Engineering, Zhejiang University, Hangzhou 310058, China
** (Corresponding author: E-mail: tonggs@zju.edu.cn)*

ABSTRACT

The hysteretic behavior of an innovative multi-cellular concrete-filled steel tube walls (CFT-walls) with tie-bolts was studied. Seven full-scale tests were conducted under constant axial loads and cyclic lateral loads. The tie-bolts were arranged to fix connectors, attach the wall studs as well as enhance the confinement between steel sheets and infill concrete. The axial compression ratio was taken be the limit which may encounter in real projects. Before the treatment of the test results, the $P-\Delta$ effect was excluded from the lateral force–drift curves as it is considered independently in the current design codes.

All the specimens presented similar spindle-shaped lateral force versus displacement hysteretic curves and failed in the severe plastic local buckling–tension cycles of the steel sheets and the crushing of concrete. No discernible pinching effect and out-of-plane buckling were observed and the specimens showed favorable hysteresis behavior, deformation capacity, and energy dissipation during the tests. The tie-bolts arranged at middle tubes and the width-to-thickness ratios of the faceplates had no discernible effect on the behavior in the investigated range. The point when the force reached two-thirds of the maximum lateral force was defined as the yield point of the member. Based on test results, two idealized backbone curves were proposed. Moreover, the hysteretic curves of all the specimens were calculated using the fiber element method and showed good agreement with the experimental results.

ARTICLE HISTORY

Received: 17 April 2020
Revised: 22 October 2020
Accepted: 26 October 2020

KEYWORDS

Composite wall;
Seismic behavior;
Experimental study;
Hysteresis characteristic;
Fiber element method

Copyright © 2021 by The Hong Kong Institute of Steel Construction. All rights reserved.

1. Introduction

Shear walls are the most common structural components that resist earthquakes or wind loads in high-rise buildings. To meet the lateral stiffness and strength demand of high-rise buildings, various composite shear walls formed of steel and concrete were proposed. The bi-steel steel–concrete–steel sandwich composite construction is one such walls[1] and is used in cores and staircase[2].

A similar type of wall, the double skin composite wall(DSC-walls) with interior studs and tie bolts(Fig.1(a)), was studied in [3,4,5]. DSC-walls are disadvantageous in that column-type local buckling occurs in the faceplates between the rows of the headed studs/tie bolts. It is well known that column-type buckling causes the loss of post-buckling strength and stiffness and decreases the vertical load capacity rapidly. Thus, Zhang et. al [6] based on a review of the experimental results from the open literature and on finite element (FE) analysis, proposed $t\sqrt{E/f_y}$ as the upper limit of the distance between the headed studs or tie bolts, where E is Young's modulus, f_y is the yield strength of steel, and t is the thickness of the faceplates. For Q355 steel, $t\sqrt{E/f_y}$ is $24t$, which is an extremely short distance for application in residential buildings. Yang et. al[7] proposed a more stringent limit on this distance.

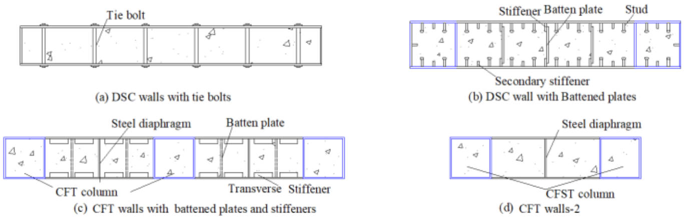

Fig. 1 Different configurations of DSC walls

Nie et. al [8] studied the cyclic behavior of DSC walls using battened plates; the cross-section of their wall is shown in Fig.1(b). Huang et. al.[9] studied the cyclic behavior of concrete-filled DSC walls using battened plates and transverse stiffeners, as shown in Fig.1(c). Guo et. al [10] conducted a static test on short concrete-filled steel tube walls (CFT-walls) to determine their vertical load capacity as well as a horizontal cyclic test on two specimens under given vertical loads. The cross-section is shown in Fig.1(d).

A new type of patented wall composed of a series of concrete-filled rectangular tubes was proposed by Hangxiao Steel Structures Corporation Limited(Patent No. CN103993682b, 2014) (hereafter, abbreviated as HX-CFT-walls). Moreover, it was applied rapidly in China in residential buildings (more than 1 million sqm have been built since 2014). The manufacture of HX-CFT-walls begins with a cold-formed square or rectangular box section; subsequently, a series of cold-formed lipped U-sections are added and welded by automatic arc welding (Fig.2(a)). After pieces of walls are manufactured, they are assembled into L- or T-shaped walls by welding either onsite or in the shop, depending on the strength demand and transportability. The wall thicknesses are 150 mm(lower stories) and 130 mm(upper stories), and the steel plate thicknesses are 5 mm and 4 mm when the heights of residential buildings are less than 80 m, the seismic ground acceleration is less than 0.2g, and the basic wind pressure is less than 0.5 $\mathrm{kN/m^2}$ (based on the maximum average wind speed of 10 min in 50 years). Thicker walls(180–400 mm) and thicker plate (6–16 mm) are required when the buildings are higher and/or the loadings are larger or the earthquakes are more severe.

Different from the bi-steel^{TM} steel–concrete–steel sandwich panels[3] and DSC-walls with studs and tie bolts[5], HX-CFT-walls have similar behavior to CFT columns. The local faceplate buckling of each cell is prohibited by restricting the width-to-thickness ratio of the faceplate to that allowed for the CFT columns. Thus, the concrete in each cell is continuously and equally confined along the height. Zhang et. al[11,12] reported cyclic tests on concrete-filled cold-formed tube walls(Figs.2(a1) and (a2)) under given axial forces. These tests verified the similarity of HX-CFT-walls and CFT columns in terms of the seismic resistance behavior.

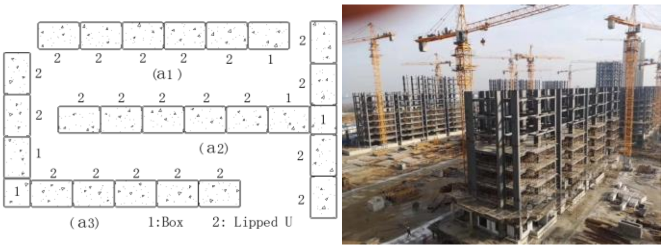

(a)Linear, L-/T-shaped CFT column T-walls (b) High-rise building using CFT-walls, Yantai, China

Fig. 2 Concrete-filled multi-cell steel tube walls and their application

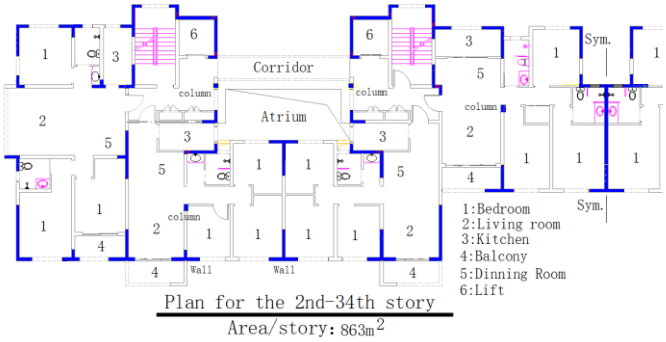

Fig. 3 Plan layout of HX-CFT walls in a residential house in Baotou, Inner Mongolia

Since cold-formed thin-walled steel sections are adopted in HX-CFT-walls, high-rise residential buildings can be built with affordable steel content, and automatic production lines have been developed so that the manufacturing costs are also reduced. Unlike DSC-walls whose applications are mainly in cores and staircases, HX-CFT-walls are arranged in plans, similar to concrete shear walls. Fig.3 illustrates a plan layout of HX-CFT-walls in a residential house of 34 stories and with a height of 97m. The street block is composed of 12 high-rise residential buildings using HX-CFT-walls and located in Baotou, Inner Mongolia, China.

However, such CFT-walls have some difficulties in attaching exterior cladding walls because welding connectors onto the cold-formed rectangular tubes with a thickness of 4–5 mm leads to permanent welding distortion. To avoid such difficulties, a modified CFT-wall, as shown in Fig.4, was proposed, in which tie-bolts are introduced to fix connectors and attach the wall studs. Tie-bolts can also increase the interfacial slip-resistant rigidity and strength between concrete and faceplates. The entire cross-section of this CFT wall is formed in such a way that a rectangular box and a cell with tie bolts are arranged alternately. Only one line of tie-bolts is used in the cells to ensure a good confining effect of the closed tubes on concrete.

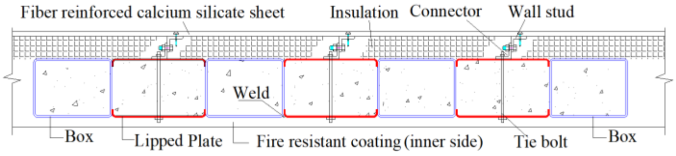

Fig. 4 CFT-walls with tie-bolts

This paper reports an experimental study on the behavior of the above mentioned modified CFT-walls with tie bolts. The bolt-to-bolt distance in the vertical direction is 0.5–0.55 times the width of the tied cell so that the local elastic buckling stress of a faceplate is 1.844–1.603 times the buckling stress of the untied plate. Thus, the width-to-thickness ratio of the cells with tie-bolts can be 20–30% greater than that of a cell without tie-bolts. The tie bolts are required to be able to withstand a lateral pressure of 2 MPa within their attribute area. A confining pressure of 2 MPa is regarded as being able to provide ductility to the infill concrete. Wider bolted cells may slightly reduce the number of welds, which is the reason for introducing this modification.

Cyclic loading tests were conducted on seven full-scale specimens. The failure mode, hysteresis loops, lateral stiffness, ductility, and energy dissipation capacity of the specimens are presented and discussed. The width-to-thickness ratios of lengthwise steel sheets are beyond the limitations recommended by Chinese codes[15] and Eurocode 4[16], which will be discussed in Section 2.1. Therefore, the effect of the tie-bolts on the buckling capacity of the steel sheets was also evaluated. Furthermore, fiber element models of the seven specimens were proposed and verified by the experimental results.

2. Experimental program

2.1. Test specimens

Seven full-scale CFT-walls with tie-bolts labeled from GHQ-1 to GHQ-7 were tested under cyclic lateral loading. The cross-sections of the specimens consist of two square boundary tubes and three or four rectangular cells. The cells next to the boundary tubes are formed by two cold-formed lipped steel sheets and tie-bolted. The middle cells are normal rectangular tubes. Flare V-groove welds with the minimum effective throat equal to the plate thickness are used to connect the tubes.

The limiting width-to-thickness ratio for square CFT columns recommended in Chinese codes[13] and Eurocode 4[14] are

$$[b/t]_{\mathrm{CECS}} = 60\varepsilon_{\mathrm{k}} \tag{1}$$

$$[b/t]_{\mathrm{EC4}} \le 52\varepsilon_{\mathrm{k}} \tag{2}$$

where b and t are the width and thickness of the steel tubes and steel sheets, respectively, and $\varepsilon_{\mathrm{k}} = \sqrt{235/f_{\mathrm{y}}}$. For $f_{\mathrm{y}} = 345\mathrm{N/mm^2}$, the $[b/t]$ limits imposed by Eqs.(1) and (2) are 49.5 and 42.9. The boundary boxes of the specimens have b/t ratios of 40 and 37.5. The width-to-thickness ratio of the second cell next to the boundary tube is determined as follows.

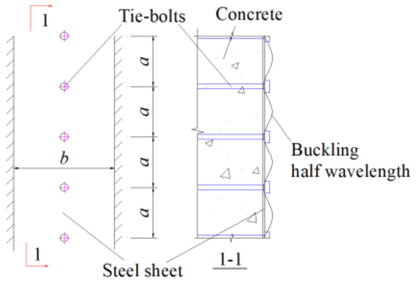

Fig. 5 Buckling of tie-bolted faceplates

Fig.5 shows a faceplate with tie-bolts; its width is b, and the distance between the tie-bolts is a. Behind the faceplate is the infill concrete, preventing the faceplate buckling toward concrete; therefore, the only possible buckling mode is shown on the right side in Fig.5. The longitudinal edges are modeled as fixed; therefore, the buckling stress of the faceplate[15] is

$$\sigma_{\mathrm{cr}} = \left(\beta^2 + \frac{2}{3} + \frac{1}{\beta^2}\right)\frac{4\pi^2 E t^2}{12(1-\mu^2)b^2} \tag{3}$$

Where $\beta = a/b$. The minimum buckling stress occurs when $\beta = 1$.

$$\sigma_{\mathrm{cr,min}} = \frac{10.667\pi^2 E t^2}{12(1-\mu^2)b^2} \tag{4}$$

If the distance a was equal to the width b, the node lines of the faceplate buckles would be automatically located at the tie-bolts, and no tie-bolts works. Therefore, the distance a is taken to be less than the width b. Table 1 lists the buckling factors for β of 0.5–1.0. The width-to-thickness ratios $(b/t)_{\mathrm{E,y}}$ for which the buckling stress is equal to $f_{\mathrm{y}} = 235$ MPa are also listed. Based on the well-known winter's formula, when the normalized width-to-thickness ratio $\lambda = \sqrt{f_{\mathrm{y}}/\sigma_{cr}}$ is equal to 0.673, the inelastic buckling strength is equal to the yield strength. The corresponding width-to-thickness ratios are also listed in Table 1. Referring to Table 1, the b/t ratio for the tie-bolted cell is set to 1.2 times that in Eq.(1), i.e., $1.2 \times 49.5 = 59.4$. The middle cells have a smaller bending stress; therefore, their b/t ratios are also set to 1.2 times that in Eq.(1) in GHQ-1/3/6/7 to check their effect.

Table1

Determination of distance between tie-bolts($f_y = 235\mathrm{N/mm^2}$, $E = 200000\mathrm{N/mm^2}$)

β	Buckling factor	$(b/t)_{\mathrm{E,y}}$	$0.673(b/t)_{\mathrm{E,y}}$	Comments
1	10.67	90.58	60.96	Based on Eq.(1)
0.8	11.48	93.96	63.23	not attractive
0.7	12.79	99.19	66.75	1.1 times in Eq.(1), not attractive for practice
0.6	15.22	108.19	72.81	1.2 times in Eq.(1), acceptable
0.55	17.10	114.69	77.18	1.29 times in Eq.(1), acceptable
0.5	19.67	122.99	82.78	1.36 times Eq.(1), acceptable

The minimum thickness of the HX-CFT-walls is taken as 130 mm, which was found to ensure the quality of concrete when the wall height was 9 m (three stories) after the concrete pouring trials. GHQ-1–6 have wall thicknesses of 130 mm, and boundary box 160×4 is introduced to improve the out-of-plane stability of the walls; concurrently, it has a limited effect on the in-plane behavior. Specimen GHQ-7 has a uniform wall thickness of 150 mm. It was demonstrated by past experience that when the wall thickness is equal to and greater than 150 mm, the out-of-plane buckling of the CFT-walls will not occur in the test.

Details of the specimens are shown in Fig.6 and listed in Table 2. Specimens GHQ-1 and GHQ-2 have identical geometries, whereas their axial force ratios, arrangement patterns of the tie-bolts, and loading histories are different. Specimens GHQ-3 and GHQ-4 have smaller width-thickness ratios than GHQ-1/GHQ-2 to examine the effect of these parameters. The middle cells of Specimens GHQ-5 and GHQ-6 have smaller widths than GHQ-4/GHQ-3, respectively.

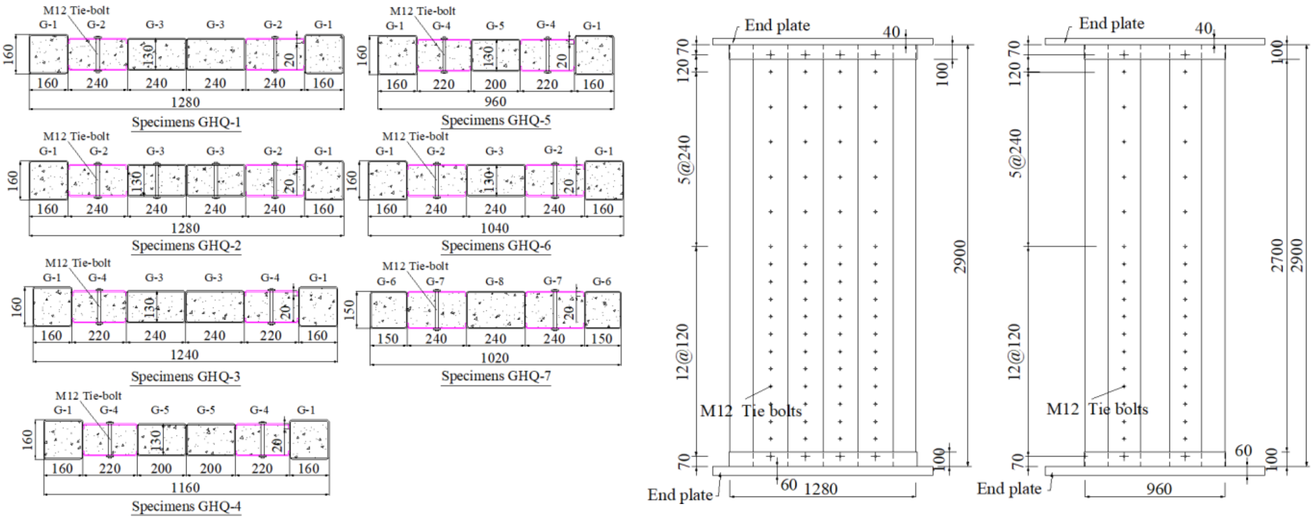

(a) Sectional configuration of specimens (b) Front view of Specimen 2 (c) Front view of Specimen 5

Fig. 6 Test specimens

Table 2

Summary of test specimens(height=2900mm)

No. GHQ	Configuration	Width-to-thickness ratio of faceplates			Wall width B (mm)	Loading history	Axial force ratio n_d / n_r	Axial force(kN)
		1stbox	2ndcell(bolted)	Mid-cell				
1	G1+G2b+G3+G3+G2b+G1	40	60	60	1280	Type 1	0.56/0.30	3450
2	G1+G2b+G3b+G3b+G2b+G1	40	60	60	1280	Type 2	0.50/0.27	3100
3	G1+G4b+G3+G3+G4b+G1	40	55	60	1240	Type 2	0.56/0.30	3350
4	G1+G4b+G5+G5+G4b+G1	40	55	50	1160	Type 2	0.56/0.30	3170
5	G1+G4b+G5+G4b+G1	40	55	50	960	Type 2	0.56/0.30	2690
6	G1+G2b+G3+G2b+G1	40	60	60	1040	Type 2	0.56/0.30	2880
7	G6+G7b+G8+G7b+G6	37.5	60	60	1020	Type 2	0.56/0.30	2880

Note: (1) Notation: "b" denotes "tie-bolted"

(2) Cell dimensions: G1: 160×160×4, G2b:130×240×4, G3,G3b:130×240×4, G4b: 130×220×4, G5:130×200×4,G6:150×150×4,G7b:150×240×4,G8:150×240×4.

Tie bolts are arranged at the center of the hollow section sections next to the boundary tubes, and the middle cells of GHQ-2 are also tie-bolted because their faceplates have a larger *b*/*t* ratio than that in Eq.(1). The distances between the tie bolts are doubled in the upper half of all the specimens because the upper parts have smaller bending moments in the tests(Figs 6(b) and (c), 240 mm and 120 mm, respectively).

The specimens have top and bottom endplates of 40 mm and 60 mm, respectively. To avoid fracture of the welds between the wall and the endplates, vertical strengthening plates 100 × 6 were attached to the wall and welded to the top and bottom of the specimens.

The limits on the normalized design axial force(defined as the ratio of the design value of the axial force and the design value of the yield strength) in the primary seismic concrete wall are taken as 0.35 and 0.4 for ductility classes DCH(high) and DCM(medium), respectively. Considering that the CFT-walls have higher ductility than concrete shear walls, for a residential building of 80 m, past experiences have revealed that the normalized design axial forces are approximately 0.5 for most CFT-walls. Therefore, it is chosen as 0.5 for all the specimens in this study.

2.2. Material properties

Table 3

Material properties of steel

Thickness (mm)	E_s (GPa)	Yield strength (MPa)	Yield strain (%)	Ultimate strength (MPa)	Ultimate strain (%)	Elongation (%)
4	208	350	0.185	495	23.4	30

Design strength grade C40 was used in all the specimens; the average cubic strength of six 150 × 150 × 150 cubic specimens of the used concrete is $f_{cu} = 54.9$ MPa and 3:1 prism strength is $f_{pr} = 0.76 f_{cu} = 41.7$ MPa . The test was conducted according to the Chinese "Standard for Test Method of Mechanical Properties on Ordinary Concrete" (GB/T 50081-2002)[16]. All the steel tubes were manufactured from Q345 steel sheets with a measured average thickness of 4.0 mm. The properties of the steel tubes, as listed in Table 3, were obtained from tensile tests conducted on coupons taken from the same batch of steel sheets.

2.3. The setup and loading procedure

All the tests were conducted using the multi-functional loading device shown in Fig.7. The specimens are bolted to the bottom block with M24(10.9s) high-strength bolts, which are clamped to the reaction floor by eight anchors. The specimens are also bolted to the top beam, which connects to the horizontal hydraulic jack. The top beam is of 400 mm in height and can distribute vertical loads to the top of the specimens. The horizontal and vertical hydraulic jacks have a capacity of 1500 kN and 25000 kN, respectively.

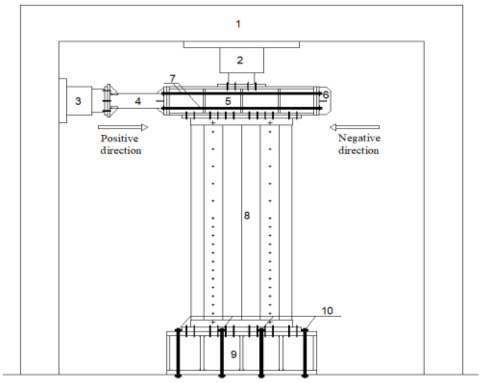

1-Steel frame, 2-Vertical hydraulic jack, 3-Horizontal hydraulic jack, 4-Left connector, 5-Top beam
6-Right connector, 7-Steel rods, 8-Specimen, 9-Foundation beam, 10-Earth anchors

Fig. 7 Test setup

The design/real axial load ratio $n_\mathrm{d}/n_\mathrm{r}$, and the corresponding axial force are listed in Table 2. The design/real axial load ratio $n_\mathrm{d}/n_\mathrm{r}$, is defined based on Eqs.(5) and (6).

$$n_\mathrm{d}=\frac{1.25N}{A_\mathrm{c}f_\mathrm{c}+A_\mathrm{s}f} \tag{5}$$

$$n_\mathrm{r}=\frac{N}{A_\mathrm{c}f_\mathrm{pr}+A_\mathrm{s}f_\mathrm{y}} \tag{6}$$

where f_pr is the prism(150 × 150 × 450) compressive strength of concrete, $f_\mathrm{pr}=0.76f_\mathrm{cu}=41.7\ \mathrm{Mpa}$, f_y is the yielding strength of the steel sheets, $f=f_\mathrm{y}/1.165$, and A_c, A_s are the areas of concrete and the steel tubes, respectively.

The axial force was first applied in five steps until the predetermined axial force was reached. The horizontal cyclic loading history was determined by the Chinese Specification of Testing Methods for Earthquake Resistant Building (JGJ 101-96)[17]. Load/displacement compound control was conducted in this test. Before the specimen yielded, the horizontal force was controlled by the load and applied in five levels, which corresponded to 1/5, 2/5, 3/5, 4/5, and 1of the predicted yield strength of the specimen. When the specimen yielded, the lateral displacement was recorded and defined as yield displacement Δy, and then the horizontal force was controlled by displacement. Two types of loading procedures were conducted during the displacement-controlled. For specimen GHQ-1, the displacement level increment corresponded to Δy, whereas it was changed to 0.5Δy in other specimen tests, as shown in Fig.8. Two circles were imposed at each displacement level, and the test was terminated when the axial force on the wall could not be maintained or the lateral load decreased below 85% of the maximum measured load capacity.

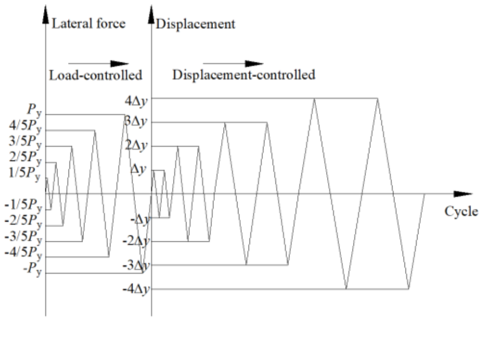

(a) Specimen GHQ-1(type 1)

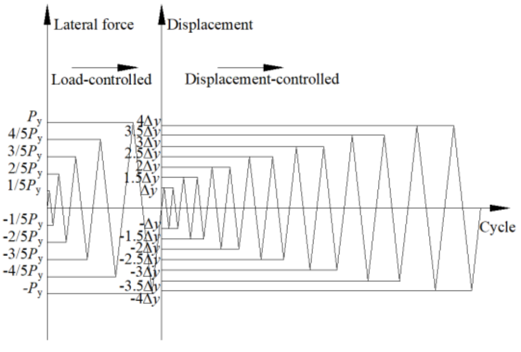

(b) Other specimens(type 2)

Fig. 8 Design loading history of specimens

2.4. Instrumentation

The instrumentation for the specimens is illustrated in Fig.9. Nine linear variable displacement transducers (LVDTs) were used. The in-plane horizontal displacements were measured by four LVDTs (H-1, H-2, H-3, and H-5) along the heights of the walls. Two LVDTs(H-6 and H-7) monitored the possible out-of-plane deformation of the specimens, and three LVDTs(H-4, V-1, and V-2) monitored the displacement of the foundation beam. The lateral and vertical loads applied by the hydraulic jack were automatically recorded by the loading system.

For recording the observations and discussing the test results, the faces of the specimens coated with a whitewash are called as front sides, and the opposite faces are defined as the back sides of the specimens. In addition, the push (horizontal hydraulic jack from left to right) is defined as positive loading, and the pull (horizontal hydraulic jack from right to left) is defined as negative loading.

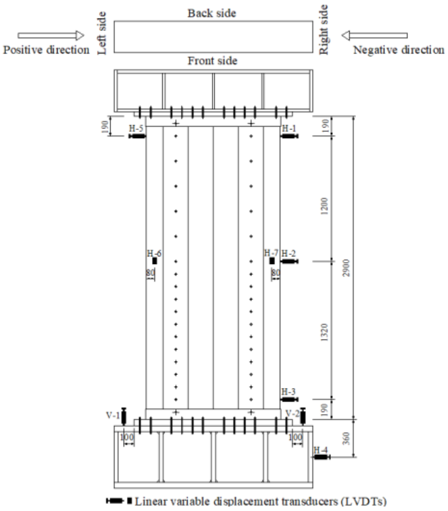

Fig. 9 Locations of LVDTs

3. Experimental results and discussion

3.1. General observations and failure modes

In general, all the specimens demonstrated similar behaviors. Taking GHQ-2 as an example, it experienced the following three stages:

Quasi-elastic stage: The P–Δ curve was approximately linear in the initial ascending part. No local buckling or physical deformation was observed. Subsequently, the specimen began to yield with some slight local buckling at the boundary tubes in the compression zone, as shown in Fig.10(a). The first plastic local buckling occurred at approximately 200 mm from the bottom of the boundary tubes in cycle Δy.

Yielding development stage: After the plastic local buckling of the boundary tube, some local buckling occurred and developed in more locations during cycles 1.5Δy to 2Δy, as illustrated in Figs.10(a) and(b). For cycle 2.5Δy, the specimen attained its ultimate strength, P_max. Noticeable local buckling was observed at a height of 350 mm in the middle tubes.

Failure stage: As the buckling of the steel faceplates became severe and the concrete crushed gradually, the lateral load decreased to $0.85P_\mathrm{max}$. The final collapse occurred with the fracture propagation of the steel profile at the buckling location (Fig.10(c)) and the crushing of concrete. The final failure mode of GHQ-2 is shown in Fig.10(d).

The failures of the other specimens are illustrated in Fig.11. During the test process, the out-of-plane deformation of the specimens was monitored by LVDTs H-6 and H-7. Except for the last circle of GHQ-1, no visible transverse displacement was observed. As Figs.10 and 11 show, the half wavelength of the steel sheets is equal to the spacing of the tie-bolts(120 mm) for the tubes with tie-bolts, indicating that the local buckling of the steel tubes was restrained and the local buckling modes were changed.

(a) Local buckling of steel sheets(2.0Δy) (b) Development of local buckling (2.5Δy) (c) Fracture propagation on the edge tube (d) Failure condition

Fig. 10 The Failure mode of Specimen GHQ-2

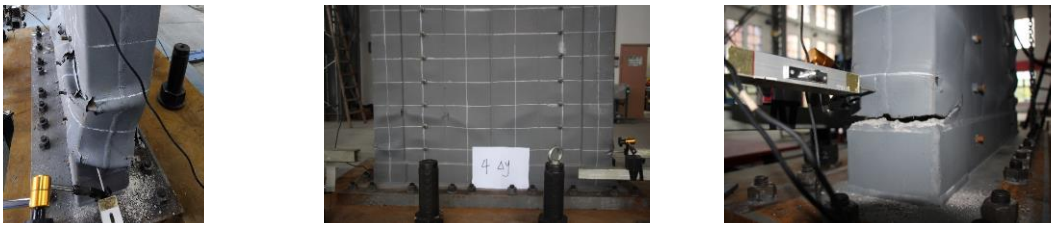

(a) Fracture propagation of steel and crushing of concrete in GHQ-1 (b) Failure condition of GHQ-3 (c) Fracture propagation in GHQ-4

(d) Failure condition of GHQ-5 (e) Failure condition of GHQ-6 from the back view (f) Local buckling waves in GHQ-7

Fig. 11 Observation of specimens

3.2. Lateral load–displacement hysteretic response

For all the tested specimens, the lateral loads versus the corresponding displacements at the top of the wall eliminating the base rotation and movement are shown in Fig.12. All the hysteretic curves are spindle-shaped, without a noticeable pinching effect. The lateral load capacities decrease because the lateral drifts are beyond the maximum load point. Degeneration of the lateral load-carrying capacity is caused by a second-order effect, concrete crushing/tensile cracking, and the local buckling of the faceplates.

The load–displacement (story drift ratio) envelope curves connect the peak points of each loading cycle on the hysteretic curves, and the results are shown in Fig.13.

The following conclusions can be obtained from Figs.12 and Fig.13:

(1) The peak loads of GHQ-1,-2 are 984 kN(GHQ-1) and 1016 kN(GHQ-2), respectively. Although GHQ-1 has larger steps, they exhibited similar behaviors, which suggested that adding tie-bolts in the middle cells has a negligible effect. GHQ-3 has a smaller b/t ratio at the tie-bolted cells than GHQ-1. The hysteretic curve is shown in Fig.12(c), and no capacity or ductility improvement over GHQ-1/2 is observed.

(2) GHQ-4 has cells with smaller width-to-thickness ratios, and improved ductility is expected. Comparing Fig.12(d) with Figs.12(a)–(c), a slightly slower degeneration of the lateral capacity is observed. The width of GHQ-4 is 9.4% smaller than that of GHQ-1/2; therefore, its maximum lateral capacity is lower.

(3) GHQ-5 has the same width-to-thickness ratio as GHQ-4; however, it has only one middle rectangular cell. Therefore, it is slender than GHQ-4. The average shear stress at the maximum lateral load is 74 N/mm^2, which is smaller than those of GHQ-1–GHQ-4. The role played by the bending moment is more dominant than that by the shear. GHQ-6 has a larger b/t ratio than GHQ-5, and its hysteretic curve is similar to that of GHQ-4.

(4) GHQ-7 with a constant wall thickness (150mm) presents a similar behavior to GHQ-6.

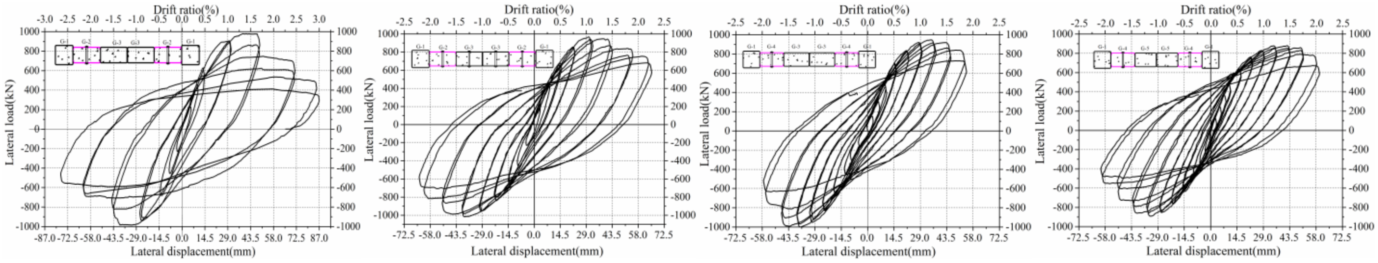

(a) Specimen GHQ-1 (b) Specimen GHQ-2 (c) Specimen GHQ-3 (d) Specimen GHQ-4

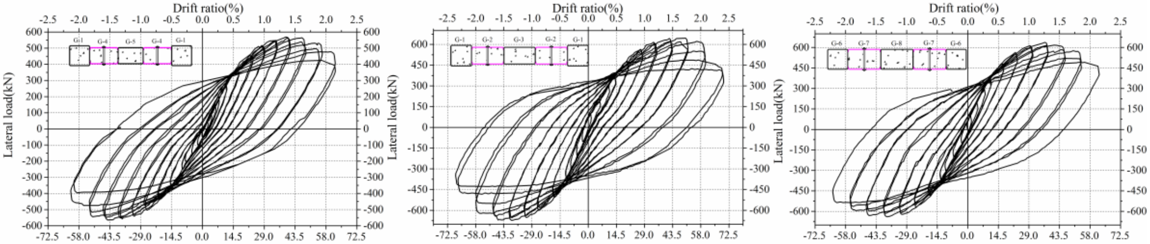

(e) Specimen GHQ-5 (f) Specimen GHQ-6 (g) Specimen GHQ-7

Fig. 12 Load–-displacement (story drift ratio) hysteresis curves of specimens

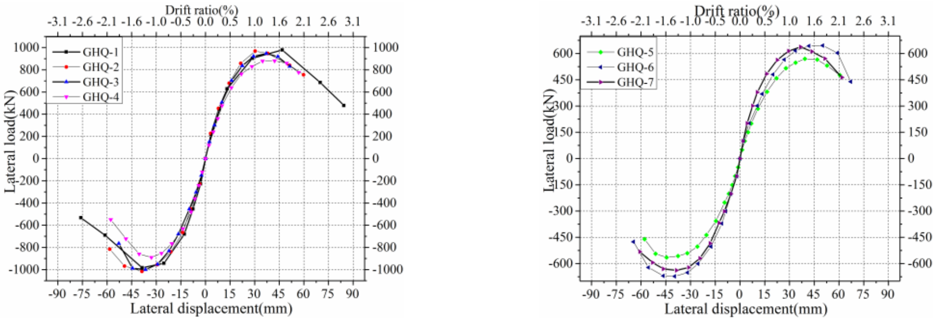

(a) Comparison of Specimens GHQ-1–GHQ-4 (b) Comparison of Specimens GHQ-5–GHQ-7

Fig. 13 Envelop curves of load—displacement

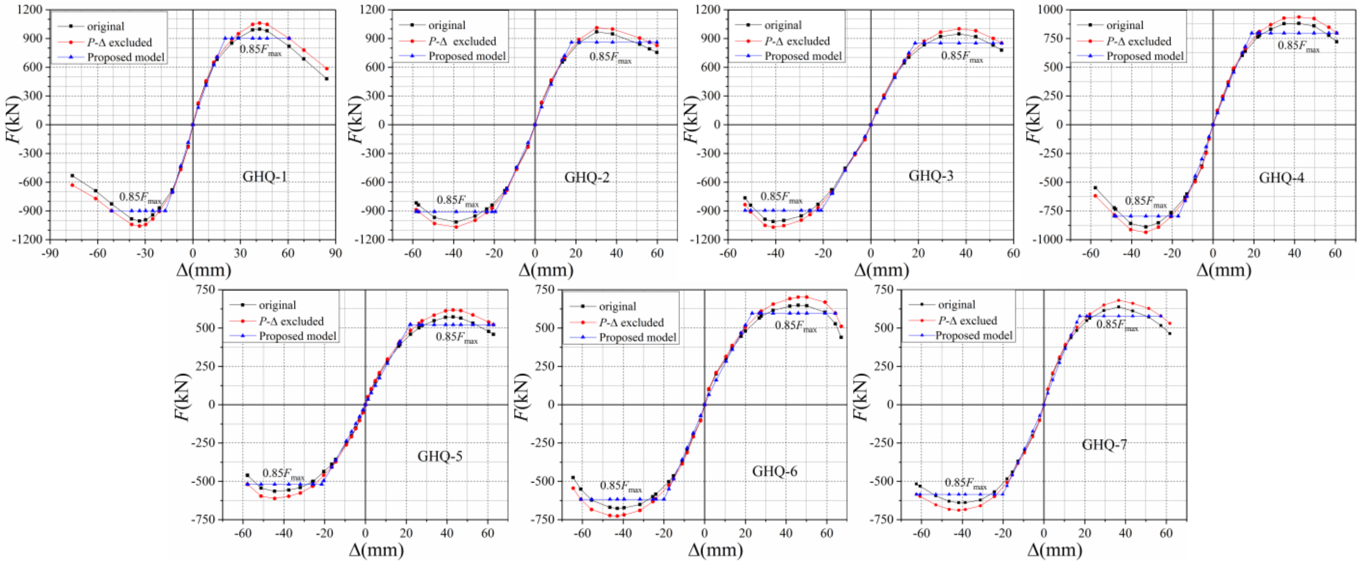

Fig. 14 Skeleton curves excluding $P-\Delta$ effect

3.3. Response curves and ductility factor excluding P–Δ effect

The hysteretic curves in Fig.12 and the skeleton curves in Fig.13 include the influences of the $P-\Delta$ effect. However, in the current design and study on the seismic behavior, this effect is isolated from the physical stiffness, as expressed in the following equilibrium equation for single-degree of freedom systems:

$$m\ddot{\Delta}+c\dot{\Delta}+F_{\mathrm{ep}}-P\Delta/h_{\mathrm{st}}=-ma_{\mathrm{g}} \tag{7}$$

Elastic–plastic hysteretic behavior is included in the term F_{ep} and the $P-\Delta$ effect is considered as an independent term; therefore, the experimental curves must be corrected to isolate the $P-\Delta$ effect.

All the seven specimens failed at their bottom; their bending moments are

$$M_{\mathrm{base}}=Ph_{\mathrm{st}}+N\Delta \tag{8a}$$

where P is the horizontal force, h_{st} is the height of the specimen, N is the axial load, Δ is the lateral displacement at the top, and M_{base} is the moment including the $P-\Delta$ moment. If the same bending moment is produced by the lateral force only, then

$$M_{\mathrm{base}}=Fh_{\mathrm{st}} \tag{8b}$$

and one obtains

$$F=P+\frac{N}{h_{\mathrm{st}}}\Delta \tag{9}$$

The corrected lateral force F—drift Δ curves for all the specimens are presented in Fig.14.

The yield displacement Δ_{y} is defined as follows: the yield strain of steel is $\varepsilon_{\mathrm{y}}=f_{\mathrm{y}}/E=350/200000=1750\mu\varepsilon$, and the strain of concrete at f_{cu} is approximately $1790\mu\varepsilon$ for C40 concrete. Both the strains are similar; therefore, the yielding point on the lateral force–displacement curves can be defined as the edge steel fiber begins to yield and the infill concrete reaches its prismatic strength. The stress diagram of this state is shown in Fig.15, and the theoretical yield moment was calculated. Table 4 lists the yield moments M_{y} of the specimens. It is found that the yield moments are approximately 0.67 times the maximum bending moment $M_{\max}=F_{\max}h_{\mathrm{st}}$; therefore, point $0.67F_{\max}$ is used as the yielding point, which is denoted by Point A in Fig. 16(c).

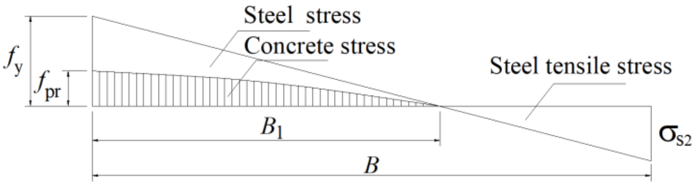

Fig. 15 Yield point definition

Connecting the origin to Point A and extending this line to $0.85F_{\max}$, the displacement of this point is denoted as $\Delta_{\mathrm{y\mu}}=(0.85/0.667)\Delta_{\mathrm{y}}=1.27\Delta_{\mathrm{y}}$. The useful limit of deformation Δ_{u} is Point C at which the lateral force drops to 85% of the maximum capacity. According to Newmark and Hall[18](Fig. 16(a)), the ductility factor is defined as

$$\mu=\frac{\Delta_{\mathrm{u}}}{\Delta_{\mathrm{y\mu}}} \tag{10}$$

Table 4
Yielding moments and components characteristics

Specimen	α_{ck}	Shear deformation percentage ξ	K_{s} (kN/m×10^6)	M_{y} (kN·m×10^6)	M_{A} ($0.67F_{\max}h_{\mathrm{st}}$) (kN/m×10^6)	$M_{\mathrm{y}}/M_{\mathrm{A}}$	ϕ_c
GHQ-1	0.596	15.5%	45.64	2327.4	2222.2	1.010	0.31
GHQ-2	0.596	15.5%	45.64	2477.3	2067.3	1.075	0.33
GHQ-3	0.595	14.8%	42.31	2202.3	2099.5	1.013	0.30
GHQ-4	0.592	12.3%	35.75	2032.5	1972.8	1.057	0.41
GHQ-5	0.586	8.7%	21.96	1247.7	1318.9	0.919	0.56
GHQ-6	0.590	10.7%	26.91	1597.2	1490.4	1.017	0.56
GHQ-7	0.612	9.4%	25.27	1466.6	1426.8	0.977	0.61

Note: $\alpha_{\mathrm{ck}}=\dfrac{A_{\mathrm{c}}f_{\mathrm{pr}}}{A_{\mathrm{s}}f_{\mathrm{y}}+A_{\mathrm{c}}f_{\mathrm{pr}}}$

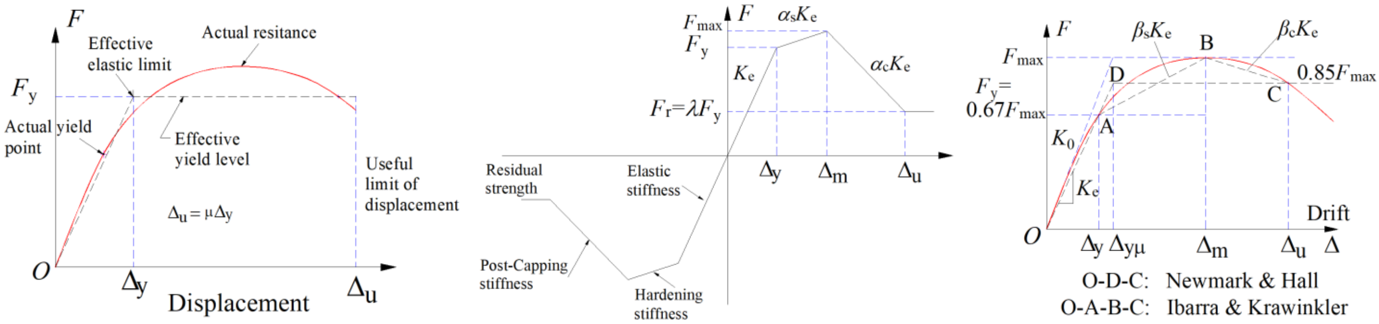

Newmark and Hall[18] (b) Ibarra and Krawinkler[19] (c) Present study

Fig. 16 Definition of ductility Factor

Table 5
Test results and parameters for Newmark and Hall’s model

Specimen	Load direction	$F_{\max}$ (kN)	$\Delta_{\mathrm{y\mu}}$ (mm)	K_0 (kN/m×10^6)	K_{e} (kN/m×10^6)	Δ_{u}	μ	Δ_{m}	$\tau_{\max}$	Δ_{y}/h	Δ_{u}/h
GHQ-1	+	1060	19.4	65.97	46.31	60.7	3.12	42.1	95.6	1/190	1/48
	−	−1058	−16.7	76.72	53.97	−51.2	3.07	−33.6	−96.1	1/222	1/57
GHQ-2	+	1012	17.0	73.12	50.43	56.2	3.30	30.3	94.6	1/217	1/52
	−	−1068	−18.9	67.15	48.15	−57.2	3.03	−38.7	−99.2	1/196	1/51
GHQ-3	+	1001	18.0	64.13	47.35	55.0	3.06	37.1	95.5	1/206	1/53
	−	−1054	−20.6	63.29	44.05	−50.5	2.45	−41.0	−100.8	1/179	1/57
GHQ-4	+	937	18.3	57.99	43.46	60.7	3.32	42.1	94.9	1/202	1/48
	−	−936	−16.4	62.77	48.49	−47.9	2.92	−33	−95.9	1/225	1/61
GHQ-5	+	614	21.6	41.45	24.30	62.8	2.91	43.0	74.2	1/171	1/46
	−	−612	−21.0	44.08	24.72	−57.7	2.75	−44.5	−73.5	1/176	1/50
GHQ-6	+	702	22.8	49.85	26.13	64.2	2.81	45.9	77.5	1/217	1/45
	−	−723	−19.4	54.02	31.78	−60.8	3.13	−42.9	−80.9	1/190	1/48
GHQ-7	+	681	17.0	53.99	34.02	57.3	3.37	36.7	78.2	1/217	1/51
	−	−684	−19.7	50.27	29.60	−62.5	3.16	−41.8	−78.3	1/187	1/46

Table 5 summarizes the lateral capacities excluding the $P-\Delta$ effect, displacements $\Delta_{\mathrm{y\mu}}$, Δ_{u}, and Δ_{m}, initial secant stiffness K_0 (computed by the first step lateral load and displacement), and secant stiffness at yield point A K_{e}. The peak load and ductility of Specimens GHQ-1 and GHQ-2 are similar, which indicates that the arrangement of the binding bars in the middle tubes(G-1) has an insignificant effect. The length of the specimens has a significant effect on the peak load and the initial lateral stiffness, whereas it has a limited effect on the ductility of the specimens.

As can be seen from Table 5, the useful drift ratios are in the range of 1/45–1/61 with the ductility factors varying from 2.45 to 3.37, which indicates that all the specimens have good ductility and exhibit ductile post-peak-load behavior as expected. Two parameters— B/h_{st}, $\tau_{\max}/f_{\mathrm{y}}$ — are correlated to the ductility factor μ, as shown in Fig.17; however, no explicit relations are found. Here, B/h_{st} is the inverse of the shear span–depth ratio, which is an important factor affecting the ductility of reinforced concrete beams and columns, $\tau_{\max}$ is the average shear stress at $F_{\max}$ neglecting the contribution of the infill concrete.

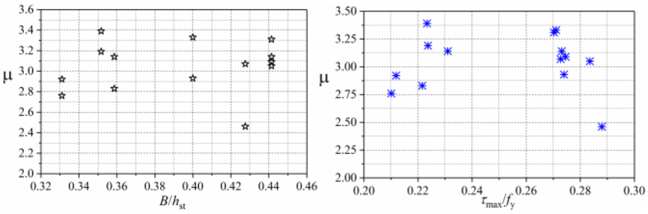

(a) (b)

Fig. 17 Correlation of ductility factors with parameters B/h_{st} and $\tau_{\max}/f_{\mathrm{y}}$

The varied factors of the seven specimens, i.e., with/without tie-bolts in the middle cells(GHQ-1 and GHQ-2) and the width-to-thickness ratios of the faceplates(50, 55, 60), have no discernible effect on the ductility.

Figs.16(b) and (c) also show a trilinear model, O–A–B–C, which was adopted by Ibarra and Krawinkler[19]. Ratios $\Delta_{\mathrm{m}}/\Delta_{\mathrm{y}}$ and $\Delta_{\mathrm{u}}/\Delta_{\mathrm{y}}$ and the parameters are listed in Table 6.

Table 6
Parameters for Ibarra and Krawinkler's model

Specimen	Load direction	$\mu_{\mathrm{m}}=\Delta_{\mathrm{m}}/\Delta_{\mathrm{y}}$	$\mu_{\mathrm{u}}=\Delta_{\mathrm{u}}/\Delta_{\mathrm{y}}$	β_s	β_c
GHQ-1	+	2.76	3.98	0.284	0.185
	−	2.57	3.92	0.318	0.167
GHQ-2	+	2.26	4.20	0.396	0.116
	−	2.61	3.87	0.309	0.180
GHQ-3	+	2.63	3.90	0.307	0.177
	−	2.53	3.12	0.321	0.378
GHQ-4	+	2.93	4.23	0.259	0.174
	−	2.56	3.72	0.320	0.195
GHQ-5	+	2.54	3.70	0.323	0.192
	−	2.70	3.50	0.295	0.281
GHQ-6	+	3.44	3.58	0.320	0.221
	−	2.81	3.99	0.274	0.191
GHQ-7	+	2.75	4.30	0.286	0.145
	−	2.69	4.03	0.293	0.167
Mean		2.70	3.95	0.308	0.198

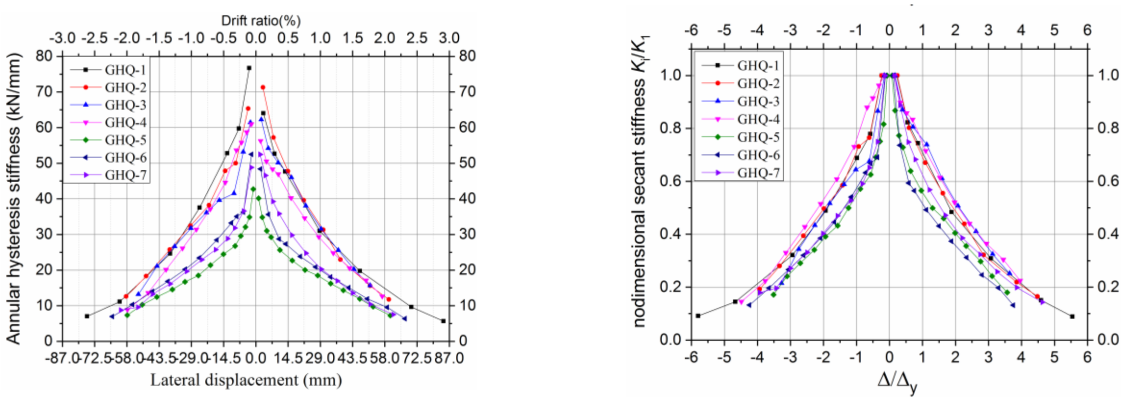

(a) Dimensional (b) Non-dimensional

Fig. 18 Stiffness degradation curves

3.4. Lateral stiffness

3.4.1. Initial stiffness and concrete reduction factor

The cross-sectional properties of the initial secant rigidity are expressed as

$$(EI)_{\mathrm{sec},0}=E_{\mathrm{s}}I_{\mathrm{s}}+\phi_{\mathrm{c}}E_{\mathrm{c}}I_{\mathrm{c}} \text{ and } (GA)_{\mathrm{sec},0}=\left(G_{\mathrm{s}}A_{\mathrm{sw}}+\phi_{\mathrm{c}}G_{\mathrm{c}}A_{\mathrm{c}}\right)/1.2,$$

where $E_{\mathrm{s}},E_{\mathrm{c}}$ are the elastic moduli of steel and concrete, respectively; $G_{\mathrm{s}},G_{\mathrm{c}}$ are the shear moduli of steel and concrete, taken as $E_{\mathrm{s}}/2.6$ and $E_{\mathrm{c}}/2.4$, respectively; $I_{\mathrm{s}},I_{\mathrm{c}}$ are the inertia moments of steel and concrete; ϕ_{c} is the reduction factor accounting for the nonlinear behavior of concrete and tensile and shear cracks of concrete; $A_{\mathrm{sw}}=2Bt$ is the steel web area of a CFT-wall, where B is the wall width and t is the thickness of the faceplates; and A_{c} is the concrete area.

The initial secant rigidities of the specimens are expressed as

$$K_0=\frac{\dfrac{3(EI)_{\mathrm{sec},0}}{h_{\mathrm{st}}^3}\cdot\dfrac{(GA)_{\mathrm{sec},0}}{h_{\mathrm{st}}}}{\dfrac{3(EI)_{\mathrm{sec},0}}{h_{\mathrm{st}}^3}+\dfrac{(GA)_{\mathrm{sec},0}}{h_{\mathrm{st}}}} \tag{11a}$$

The yield point secant rigidity is

$$K_{\mathrm{e}}=\frac{\dfrac{3(EI)_{\mathrm{sec,y}}}{h_{\mathrm{st}}^3}\cdot\dfrac{(GA)_{\mathrm{sec,y}}}{h_{\mathrm{st}}}}{\dfrac{3(EI)_{\mathrm{sec,y}}}{h_{\mathrm{st}}^3}+\dfrac{(GA)_{\mathrm{sec,y}}}{h_{\mathrm{st}}}} \tag{11b}$$

K_0 and K_{e} are calculated based on the test results and are summarized in Table 5. Ratio K_{e}/K_0 is within 0.6–0.7. The theoretical rigidity considering only steel is

$$K_{\mathrm{s}}=\frac{\dfrac{3EI_{\mathrm{s}}}{h_{\mathrm{st}}^3}\cdot\dfrac{GA_{\mathrm{sw}}}{h_{\mathrm{st}}}}{\dfrac{3E_sI_{\mathrm{s}}}{h_{\mathrm{st}}^3}+\dfrac{GA_{\mathrm{sw}}}{h_{\mathrm{st}}}} \tag{11c}$$

K_{s} is also provided in Table 4. It was found that K_{e} is only slightly greater than K_{s}, which suggests that the contribution of concrete to the lateral stiffness is small.

Based on the initial secant stiffness of the tested specimens, the reduction factor ϕ_{c} is computed and listed in Table 4, which is within 0.3–0.6. It is found that the specimens with smaller B/h_{st} (bending deformation dominant) having a larger ϕ_{c}. In addition, the initial shear deformation values in percentage ξ listed in Table 4 were computed as follows:

$$\xi=\frac{\dfrac{3(EI)_{\mathrm{sec},0}}{h_{\mathrm{st}}^3}}{\dfrac{3(EI)_{\mathrm{sec},0}}{h_{\mathrm{st}}^3}+\dfrac{(GA)_{\mathrm{sec},0}}{h_{\mathrm{st}}}} \tag{12}$$

3.4.2. Stiffness degradation

The stiffness of the specimens decrease gradually as the lateral displacement and test circles increase, which is mainly due to the cumulative plastic damage during the test. To investigate the stiffness degradation of the specimens, secant hysteresis stiffness K_i is defined as

$$K_i=\frac{\left|\pm P_i\right|}{\left|\pm y_i\right|} \tag{13}$$

where K_i is the annular hysteresis stiffness of the *i*th cycle at the displacement level of I, and P_i, y_i are the maximum lateral force and the corresponding displacement of the ith cycle at the displacement level of I, respectively.

Figs.18(a) and (b) show the dimensional and non-dimensional stiffness degradation of the specimens at various displacements (drift ratios), respectively. The initial annular stiffness is mainly controlled by the bending stiffness around the cross-sectional strong axis of the specimens when the other parameters are the same. Fig.18(b) shows that the stiffness of the slenderer specimens(GHQ-5 to GHQ-7) decreases more steeply after the specimens yield.

3.5. Energy dissipation capacity

The energy dissipated at each loading level can be measured as the area enclosed by the hysteresis loop. An equivalent hysteretic damping coefficient, h_e[20], is used in this study to evaluate the energy dissipation capacity of the specimens, as expressed in Eq. (14).

$$h_e = \frac{1}{2\pi}\frac{S_{\mathrm{ABCDEF}}}{S_{\Delta\mathrm{OCH}} + S_{\Delta\mathrm{OFG}}} \tag{14}$$

where S_{ABCDEF} is the area enclosed by the hysteresis loop indicated in Fig.19, S_{OCH} and S_{OFG} are the areas of triangles OCH and OFG(the shadowed areas), respectively, illustrated in the inset of Fig.19. These areas are computed, and the equivalent hysteretic damping coefficients h_e of the specimens are depicted in Fig.19.

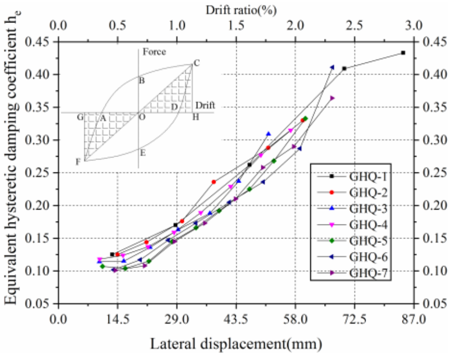

Fig. 19 Energy dissipation capacity of specimens

As expected, h_e increases with increasing lateral displacement. Before the yielding of the specimens, the values of the coefficient are approximately 0.10. During the yielding development stage, it ranges from 0.10 to 0.15. The final equivalent damping coefficients of all the specimens are over 0.3, which indicates that the specimens have good energy dissipation capacity. As all the specimens have similar values of equivalent damping coefficients, the configuration of the shear walls has a limited effect on the energy dissipation capacity of the specimens.

4. Fiber element method

The fiber element method is a highly efficient numerical scheme for simulating the monotonic and cyclic behaviors of composite cross-sections, including circular[21] and square CFT columns[22,23,24] and concrete-filled double-skin steel-plate composite walls[25]. In the fiber element model, the cross-section components are discretized into small fibers, as shown in Fig.20, and the uniaxial stress–strain curves are used for each fiber of the cross-section. Compared to the conventional finite element method, the fiber element method has a lower computational cost with fewer degrees of freedom because only sectional fibers are required in the analysis. Hence, the fiber element method was employed to simulate the cyclic performance of the seven specimens in this study.

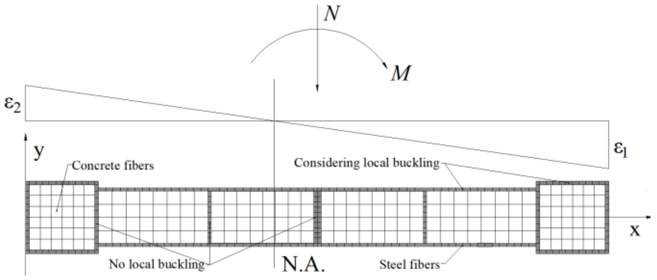

Fig. 20 Discretization of composite shear walls

In addition, the following assumptions are made in the analysis:

(1) Plane sections of the concrete core and steel sheets remain plane, and the material fibers in the cross-section are subjected only to the uniaxial stress states during the analysis.

(2)The slip between the concrete and a steel tube is not considered which was demonstrated to have little effect on the strength[26].

(3)The tensile strength of concrete and the effects of creep and shrinkage are neglected.

(4) The effects of concrete confinement and tie-bolts on the strength and ductility are considered in the stress–strain model for confined concrete[27,28].

(5) The shear deformation of a double-skin-profiled composite shear wall was studied by Nie[29] and Zhang[30], who found that the shear deformations accounted for approximately 20% of the total deformation when the shear span ratio of the wall was 2.0. As discussed in Section 3.4.1, the shear deformation accounts for 10%–15% of the total lateral deformation(Table 4) in the very initial state. In the late stage, it was found that the shear modulus of concrete rapidly drops to zero[31], and the shear deformation contributes a greater part to the total lateral deformation. In this study, it is assumed that the shear deformation percentage in the total deformation is doubled in the late stage, i.e., 30% for GHQ-1–3, 25% for GHQ-4, and 20% for GHQ-5–7.

The stress–strain relationships of the confined concrete and steel sheets are shown in Fig.21; they consist of two parts: (1) a monotonic behavior during compression and tension, and (2) hysteresis rules governing the behavior under cyclic loading. For the confined concrete, the effect of the tie-bolts on the concrete core, such as the concrete in G-2 of Specimen GHQ-1, was considered using the material model proposed by Long and Cai[27]. Considering the local buckling of the steel sheets, as shown in Fig.20, the stress–strain relationship incorporating a descending stage proposed by Thai[32] was used to determine the post-local buckling behavior of the steel sheets. The main parameters and formula are presented in Fig.21, and more details on the stress–strain relationships of the confined concrete and steel sheets can be found in the papers by Marder[28], Liang[33], and Shi[34].

The hysteretic and envelop curves calculated by the fiber element method are compared to the experimental results, as shown in Fig.22, and a good agreement is found. In addition, the yield and inelastic local buckling points of the edge steel fiber were obtained. The fiber element models have slightly higher lateral stiffness than the experimental values, which may be owing to the assumption of shear deformations of the shear walls, local bending of the faceplates, and slippage of the foundation beam and bolts, as discussed by Han[35]. The fiber element method used in this study is effective with reasonable accuracy; however, the weld cracks and thereby the loss of strength in both the nearby steel and concrete cannot be incorporated into the model. This is the cause of the difference between the method and experimental results in the late post-peak stage.

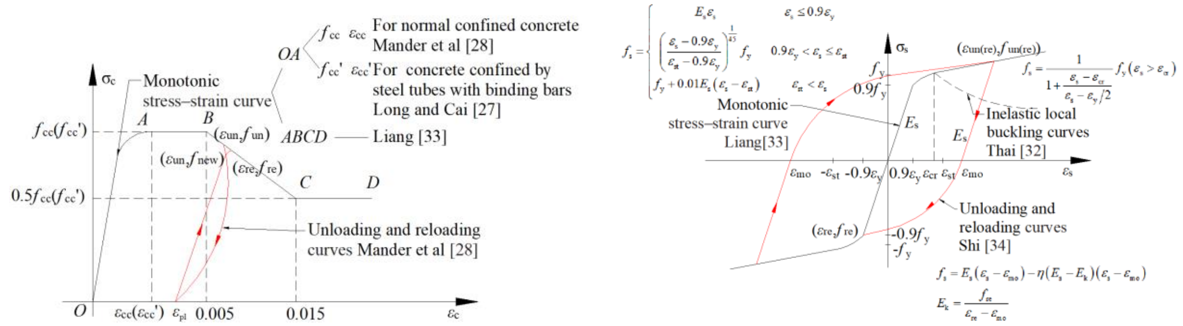

(a) Confined concrete

(b) Steel sheets

Fig. 21 Stress–strain relationship of confined concrete and steel sheets

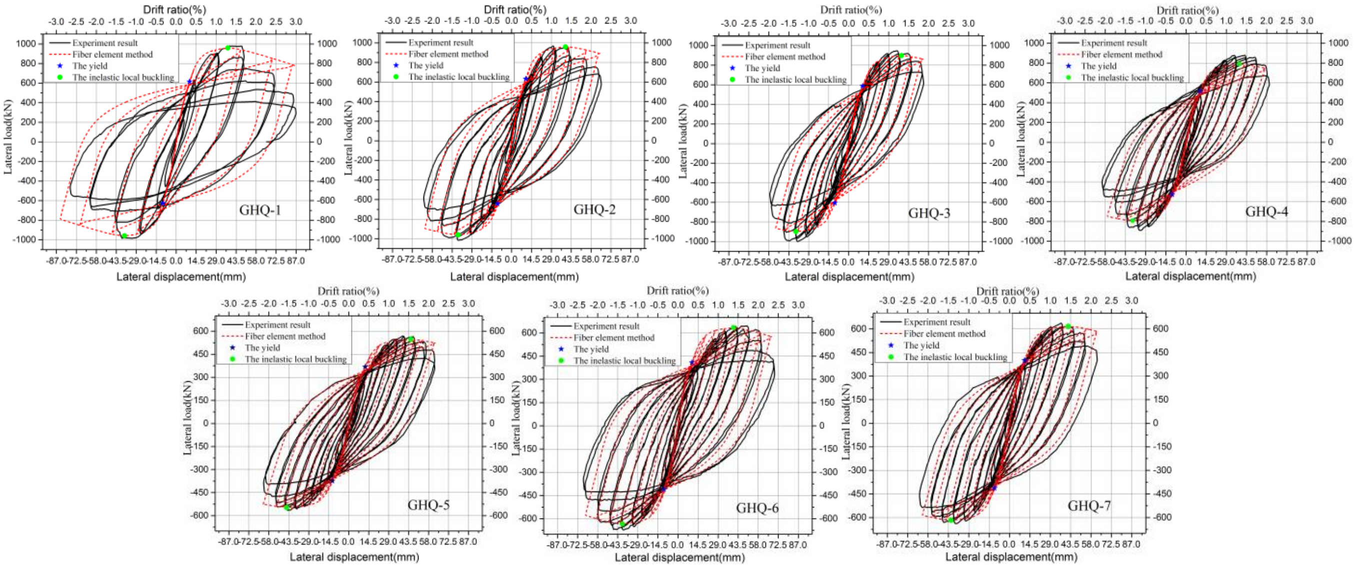

Fig. 22 Comparison between experimental hysteretic curves and calculated curves

5. Summary and conclusions

In present study, the hysteretic behavior of an innovative multi-cellular CFT-walls with tie-bolts was studied. Seven full-scale tests were conducted under constant axial and cyclic lateral loads. The axial force was taken to be the limit used in practice. The width-to-thickness ratios of the faceplates and the total width of the walls were varied among the specimens.

Before the treatment of the test results, the $P-\Delta$ effect was excluded from the lateral force–drift curves because the $P-\Delta$ effect is considered independently in the current design codes.

The following conclusions can be drawn:

(1) All the specimens show similar hysteretic behaviors and failure patterns during the tests. The lateral force versus displacement hysteretic curves are spindle-shaped without a discernible pinching effect, which indicates that the specimens have favorable hysteresis behavior, deformation capacity, and energy dissipation.

(2) Failure was triggered by the plastic local buckling of the faceplates and the tensile cracks of the cold-formed corner after repeated tension and local buckling. As the buckling deformation of the steel faceplates became severe and the concrete crushed gradually, the specimens failed during the fracture propagation of the steel profile and the crushing of the concrete.

(3) Based on the experimental observations, the tie-bolts can suppress the local buckling half-wavelength of the steel sheets, validating the design method of the specimens.

(4) The presence of tie-bolts in the middle tubes (G-1) of Specimen GHQ-2 has an insignificant effect on the peak load and ductility of the specimens owing to a low stress distribution. This suggests that the tie-bolts may not be present in the middle cells, even if the middle cells have a larger width-to-thickness ratio than that in the edge CFT columns.

(5) The width-to-thickness ratios of the faceplates have no discernible effect on the behavior in the investigated range (50, 55, 60) when the boundary tubes are the same.

(6) Two idealized models for the hysteretic curves were proposed. One was Newmark and Hall's model, in which the average ductility factor of the specimens is 3.10. The second was Ibarra and Krawinkler's trilinear model, in which the average "peak drift/yield drift" ductility is 2.70 and the average "useful drift/yield drift" ratio is 3.95.

(7) The hysteretic and envelop curves calculated by the fiber element method are compared to the experimental results, and a good agreement is found.

References

[1] Pryer J.W. and Bowerman H.G., "The development and use of British steel bi–steel", Journal of Constructional Steel Research, 46(1-3), 15-0, 1998.

[2] Gough V. and Grubb K., "Fast Steel cores", Modern Steel Constrction, AISC, June, 2007.

[3] Bowerman H.G. and Chapman J.C., "Bi-steel^{TM} steel-concrete-steel sandwich construction", Composite Construction in Steel and Concrete IV, 656-667, 2002.

[4] McKinley B. and Boswell L.F., "Behaviour of double skin composite construction", Journal of Constructional Steel Research, 58 (10), 1347-1359, 2002.

[5] Eom T.S., Park H.G., Lee C.H., Kim J.H. and Chang I.H., "Behavior of double skin composite wall subjected to in-plane cyclic loading", Journal of Structural Engineering, 135 (10), 1239-1249, 2009.

[6] Zhang K., Varma A. H., Malushte S. R. and Gallocher S., "Effect of shear connectors on local buckling and composite action in steel concrete composite walls", Nuclear Engineering and Design, 269, 231– 239, 2014.

[7] Yang Y., Liu J.B. and Fan J.S., "Buckling behavior of double-skin composite walls: An experimental and modeling study", Journal of Constructional Steel Research, 121, 126–135, 2016.

[8] Nie J.G., Hu H.S., Fan J.S., Tao M.X., Li S.Y. and Liu F.J., "Experimental study on seismic behavior of high-strength concrete filled double-steel-plate composite walls", Journal of Constructional Steel Research, 88, 206-219, 2013.

[9] Huang S.T., Huang Y.S., He A., Tang X.L., Chen Q.J., Liu X.P. and Cai J., "Experimental study on seismic behaviour of an innovative composite shear wall", Journal of Constructional Steel Research,148, 165-179, 2018.

[10] Guo L.H., Wang Y.H. and Zhang S.M., "Experimental study of rectangular multi-partition steel-concrete composite shear walls", Thin Walled Structures, 130, 577-592, 2018.

[11] Zhang X.M., Qin Y. and Chen Z.H., "Experimental seismic behavior of innovative composite shear walls", Journal of Constructional Steel Research, 116, 218-232, 2016.

[12] Zhang X.M., Qin Y., Chen Z.H. and Jie L., "Experimental behavior of innovative T-shaped composite shear walls under in-plane cyclic loading", Journal of Constructional Steel Research, 120, 143-159, 2016.

[13] T/CECS 546-2018, Technical standard for structures with concrete-filled multi-cellular steel tube walls, China Association for Engineering Construction Standardization, China JiHua Press,2018

[14] Eurocode 4, Design of composite steel and concrete structures, Part 1.1: General rules and rules for buildings, British Standards Institution, London, 1994.

[15] P.S. Bulson, The Stability of flat plates, Chatto&Windus, London, 1970.

[16] GB/T50081-2002, Test Method of Mechanical Properties on Ordinary Concrete, China Ministry of Construction, Beijing, 2003.

[17] JGJ 101-96, Specification of Testing Methods for Earthquake Resistant Building. China Planning Press, Beijing, 1997.

[18] Newmark N. M. and Hall W.J., "Earthquake spectra and design", Earthquake Engineering Research Institute, 1982.

[19] Ibarra L. F., MedinaR. A. and Krawinkler H, "Hysteretic models that incorporate strength and stiffness deterioration", Earthquake Engineering and Structural Dynamics. 34, 1489-1511, 2005.

[20] Nie J.G., Fan J.S., Liu X.G. and Huang Y., "Comparative study on steel plate shear walls used in a high-rise building", Journal of Structural Engineering, 139(1), 85-97, 2012.

[21] Liang Q.Q., "Nonlinear analysis of circular double-skin concrete-filled steel tubular columns under axial compression", Engineering Structures, 131, 639-650, 2017.

[22] Patel V.I., Liang Q.Q. and Hadi M.N.S, "Numerical analysis of high-strength concrete-filled steel tubular slender beam-columns under cyclic loading", Journal of Constructional Steel Research, 92, 183-194, 2014.

[23] Zubydan A.H. and Elsabbagh A.I., "Monotonic and cyclic behavior of concrete-filled steel-tube beam-columns considering local buckling effect", Thin WalledStructures.49 (4), 465-481, 2011.

[24] Wang Y.T., Cai J. and Long Y.L., "Hysteretic behavior of square CFT columns with binding bars", Journal of Constructional Steel Research, 131, 162-175, 2017.

[25] Hu H.S., Nie J.G. and Eatherton M.R., "Deformation capacity of concrete-filled steel plate composite shear walls", Journal of Constructional Steel Research, 103, 148-158, 2014.

[26] Hajjar J. F., Schiller P. H. and Molodan A., "A distributed plasticity model for concrete-filled steel tube beam-columns with interlayer slip", Engineering Structures, 20 (8), 663-676, 1998.

[27] Long Y.L. and Cai J., "Stress–strain relationship of concrete confined by rectangular steel tubes with binding bars", Journal of Constructional Steel Research, 88, 1-14, 2013.

[28] Mander J.B., Priestley M.J.N. and R. Park, "Theoretical stress–strain model for confined concrete", Journal of Structural Engineering, ASCE, 114(8), 1804–26, 1988.

[29] Nie J.G., Ma X.W., Tao M.X., Fan J.S. and Bu F.M., "Effective stiffness of composite shear wall with double plates and filled concrete", Journal of Constructional Steel Research, 99, 140-148, 2014.

[30] Zhang X.M., Experimental study and theoretical analysis on seismic performance of composite shear wall with steel tubes and filled concrete, Tianjin University, Tianjin, 2016.

[31] Rahal K. N., "Post-cracking shear modulus of reinforced concrete membrane elements", Engineering Structures, 32(1), 218-225, 2010.

[32] Thai H.T., Uy B. and Khan M., "A modified stress-strain model accounting for the local buckling of thin-walled stub columns under axial compression", Journal of Constructional Steel Research, 111, 57-69, 2015.

[33] Liang Q.Q., "Performance-based analysis of concrete-filled steel tubular beam columns, part I: theory and algorithms", Journal of Constructional Steel Research, 65(2), 363–72, 2009.

[34] Shi G., Wang M., Bai Y., Wang F., Shi Y.J. and Wang Y.Q., "Experimental and modeling study of high-strength structural steels under cyclic loading", Engineering Structures. 37, 1–13, 2012.

[35] Han W.L., "Discussion on "Experimental seismic behavior of innovative composite shear walls" by Xiaomeng Zhang, Ying Qin and Zhihua Chen [J Constr Steel Res 2016; 116(1): 218–232] and "Experimental behavior of innovative T-shaped composite shear walls under in-plane cyclic loading" by Xiaomeng Zhang, Ying Qin, Zhihua Chen and Li Jie [J Constr Steel Res 2016; 120(4): 143–159]", Journal of Constructional Steel Research, 147, 187–190, 2018.